J Mater Sci (2019) 54:10204–10216

Composites

Preparation of manganese porphyrin/niobium tungstate nanocomposites for enhanced electrochemical detection of nitrite

Zichun Fan[1,2], Liuxue Sun[1,2], Shining Wu[1,2], Chao Liu[3,*], Mengjun Wang[1,2], Jiasheng Xu[1,2], Xiaobo Zhang[1,2], and Zhiwei Tong[1,2,4,*]

[1] School of Chemical Engineering, Huaihai Institute of Technology, Lianyungang 222005, China
[2] Jiangsu Key Laboratory of Function Control Technology for Advanced Materials, Huaihai Institute of Technology, Lianyungang 222005, China
[3] School of Materials Engineering, Yancheng Institute of Technology, Yancheng 224051, China
[4] SORST, Japan Science and Technology Agency (JST), Kawaguchi Center Building 4-1-8, Kawaguchi-shi, Saitama 332-0012, Japan

Received: 8 January 2019
Accepted: 8 March 2019
Published online: 12 April 2019

ABSTRACT

The sandwich-structured MnTMPyP/$NbWO_6$ nanocomposites were synthesized by the electrostatic self-assembly of the manganese porphyrin (MnTMPyP) cations with the exfoliated niobium tungstate $[NbWO_6]^-$ nanosheets. Various analytical techniques such as X-ray diffraction patterns, scanning electron micrograph, transmission electron microscope, energy-dispersive spectroscopy, UV–Vis absorption spectra and Fourier transform infrared spectra were used to determine the structure, composition and morphology of the as-prepared samples. It can be concluded that MnTMPyP cations were inserted into interlayer spacing of the $[NbWO_6]^-$ nanosheets and arranged in an inclined single layer at 58°. The MnTMPyP/$NbWO_6$ nanocomposites modified electrode exhibited excellent electro-catalytic oxidation activity toward nitrite in 0.2 mol L^{-1} and pH 7.0 phosphate buffer solution. Additionally, the oxidation peak current is proportional to the square root of scan rates, indicating that the redox reaction of nitrite is a typical diffusion-controlled process. Also, the sensitivity and detection limit for nitrite at the modified electrode was evaluated as 3.80×10^{-5} mol L^{-1} over a concentration range from 1.20×10^{-4} to 3.57×10^{-3} mol L^{-1} by using differential pulse voltammetry.

Address correspondence to E-mail: cliu@ycit.edu.cn; zhiweitong575@hotmail.com

https://doi.org/10.1007/s10853-019-03526-4

Introduction

Nitrite is a kind of the widespread inorganic pollutant in environment, agriculture and chemical industry. It is also a common additive and preservative in the food industry [1–3]. Nitrite can react with hemoglobin in the blood to form methemoglobin, and the process is irreversible, leading to insufficient oxygen supply to the body [4, 5]. As a result, nitrite as a potentially toxic substance is harmful to the human health. This has also drawn the attention of the World Health Organization, which has set a maximum of 1 mg L^{-1} nitrite in drinking water [6]. Hence, the quantitative analysis of nitrite becomes particularly important.

So far, various analytical techniques have been used for the detection of nitrite, such as electrochemical sensor [7, 8], fluorescent spectroscopy [9], spectrophotometry [10], capillary electrophoresis [11] and chromatography [12]. Among the above analytical techniques, the electrochemical testing method attracts more attention and is widely adopted to detect nitrite owing to advantages of simple, convenient, inexpensive, high sensitivity and great selectivity [13–15].

In recent years, more and more layered metal oxide semiconductors (LMOSs) were focused due to their unique layered structure, ion-exchange capacity, superior thermal stability and great electrical conductivity, such as $KTiNbO_5$ [16, 17], $CsTi_2NbO_7$ [18], $LiTaWO_6$ [19], $LiNbWO_6$ [20]. In consideration of the above advantages, a lot of modified electrodes based on these LMOSs have been prepared to study their applications in the field of electrochemistry [21–23]. However, the pure LMOSs are not suitable for the direct detection in electrochemical experiments because they exhibit very weak electrochemical activity and rather-low efficiency. Hence, some effective measures should be taken to enhance the performance of LMOSs. According to some previous reports [24–26], LMOSs were used as the host materials, and their negatively charged nanosheets can be obtained successively through acidification and exfoliation processes. A number of positively charged species have been discovered and introduced into the negative nanosheet layers by using electrostatic self-assembly technique, such as methylene blue cation [27] and metalloporphyrin cation [28]. The properties of the acquired nanocomposites can be improved, and the prepared electrochemical sensors are very stable. Moreover, this technology possesses the merits of quick, reliable, practical and simple operation.

As an important natural compound, porphyrins and porphyrin derivatives exist widely in biological systems and have regulated structure and outstanding properties [29, 30]. In addition, metalloporphyrin exhibits prospective application in electrochemical sensors as a consequence of its superior electro-catalytic capability for molecular oxygen reduction [31, 32]. As a result, various porphyrin-based modified electrodes have been performed in detection of nitrite [33], oxygen [34], ascorbic acid [35] and other biochemicals. Thereby the nanocomposites formed by the immobilization of porphyrin derivatives in various LMOSs have focused the attention of researchers.

In this study, $LiNbWO_6$ with orthorhombic structure was selected to be host material, and the corresponding schematic structure of it is shown in Fig. S1 [20]. Also, MnTMPyP was chosen as guest material. Therefore, the MnTMPyP/$NbWO_6$ nanocomposites were synthesized by combining the host $[NbWO_6]^-$ nanosheets with the guest MnTMPyP cations via the exfoliation/restacking method. A novel and sensitive nanocomposites-based electrochemical sensor was developed to determine the nitrite. The as-prepared samples were characterized by X-ray diffraction (XRD), scanning electron micrograph (SEM), transmission electron microscope (TEM), energy-dispersive spectroscopy (EDS), infrared vibrational spectroscopy and UV–Vis spectroscopy. Furthermore, the MnTMPyP/$NbWO_6$ modified electrode reveals excellent electro-catalytic oxidation activity, stability and anti-interference toward nitrite via cyclic voltammetry (CV) and differential pulse voltammetry (DPV). The results indicate that the proposed modified electrode shows promising application in electrochemical sensor.

Experimental

Exfoliation of niobium tungstate nanosheets

A traditional solid-state method was employed to synthesize layered $LiNbWO_6$ according to the previous literature [36]. The $LiNbWO_6$ was obtained by calcining stoichiometric mixture of Li_2CO_3 (Sinopharm), Nb_2O_5 (Sinopharm) and WO_3 (Sinopharm) with molar ratio of 1:1:2 at 800 °C in air for 12 h twice. The as-prepared $LiNbWO_6$ (2 g) was treated

with 2 mol L^{-1} HNO_3 aqueous solution (60 mL) at room temperature for 3 days and replaced with a fresh acid solution every day during the proton exchange reaction. The protonated product ($HNbWO_6$) was centrifugal washed three times to remove the excess NO_3^-, and then dried at 80 °C in a vacuum oven overnight. In order to obtain $[NbWO_6]^-$ nanosheets [37], 0.1 g of acidified product $HNbWO_6$ was added to a solution containing 42 mL of distilled water and 700 μL of tetrabutylammonium hydroxide (TBAOH, 10% in water). After stirring for a week, a translucent colloidal dispersion was obtained. The resulting colloidal dispersion was centrifuged at 9000 rpm for 10 min to remove the unexfoliated particles. The supernatant solution is $[NbWO_6]^-$ nanosheets.

Self-assembly of $[NbWO_6]^-$ nanosheets and MnTMPyP

To obtain MnTMPyP/$NbWO_6$ nanocomposites, 1 mmol L^{-1} MnTMPyP aqueous solution was evenly dispersed in the $[NbWO_6]^-$ nanosheets colloidal solution with a volume ratio of 1:1 between MnTMPyP aqueous solution and $[NbWO_6]^-$ nanosheets. After shaking, large amounts of brown precipitate were generated, owing to the electrostatic self-assembly of cationic MnTMPyP cations and the anionic $[NbWO_6]^-$ nanosheets. After settling for 2 h, the precipitate of MnTMPyP/$NbWO_6$ was centrifuged at 9000 r min^{-1} for 5 min, washed with distilled water for 3 times and then dried at 50 °C in a vacuum oven for 24 h.

Fabrication of MnTMPyP/$NbWO_6$ nanocomposites modified electrode

Two milligrams of MnTMPyP/$NbWO_6$ nanocomposites were dispersed in 1 mL distilled water and then treated with ultrasonic treatment for 30 min. Then, 7 μL of the obtained suspension was taken to coat on the surface of the glassy carbon electrode (GCE). The modified GCE is denoted as MnTMPyP/$NbWO_6$/GCE.

Characterization

A RINT 2000 diffractometer (Rigaku Corporation, Tokyo, Japan) by using Cu Kα radiation (λ = 0.154 nm) with 2θ going from 1.5° to 70° was collected to obtain XRD data. Analysis of element types and contents of nanocomposite was measured by EDS equipped with a FEI Tecnai G2F30S-TWIN transmission electron microscope. SEM images of the Au-coated samples were acquired with a JSM-5600 apparatus (JEOL). TEM image of nanocomposite was photographed with a JEM-2010 instrument (JEOL). Atomic force microscope (AFM) image was taken with a Bruker dimension edge SPM equipment. Britain's Malvern Zetasizer Nano instrument was used to monitor the Zeta potential value of nanosheets colloidal dispersion. FT-IR spectra were recorded by FTIR-8400S spectrometer (Shimadzu Corporation, Japan) with KBr pellets. UV–Vis absorption spectra were measured by a UV–Vis spectrometer (UV-2550). CV and DPV measurements were taken in a CHI660C electrochemical workstation with a conventional three-electrode system including saturated calomel electrode (SCE), platinum wire electrode and glassy carbon electrode (GCE).

Results and discussion

XRD analysis

The XRD patterns of the obtained products are shown in Fig. 1. $LiNbWO_6$ is orthorhombic structure, space group P-421 m, lattice parameters $a = b =$ 0.4681 nm and c = 0.9275 nm [20]. It can be clearly seen that the original $LiNbWO_6$ has narrow and strong diffraction peaks, indicating its well crystallinity. A characteristic (001) peak of $LiNbWO_6$ is at

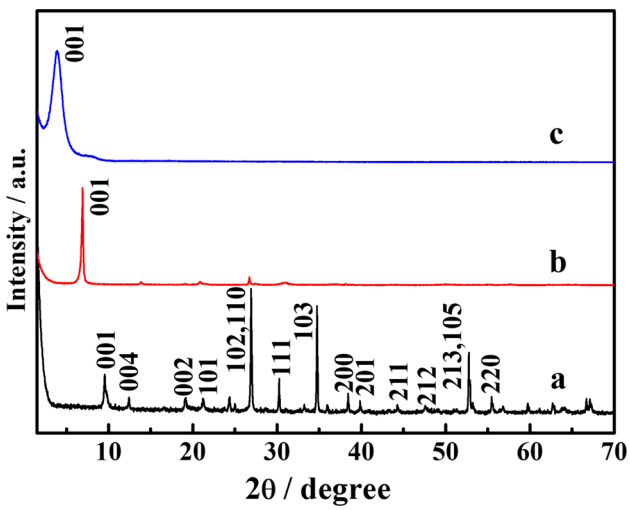

Figure 1 XRD patterns of (a) $LiNbWO_6$, (b) $HNbWO_6$, (c) MnTMPyP/$NbWO_6$.

9.56°, which is in accordance with the standard XRD data (JCPDS 84-1764) [38]. An exchange of Li^+ with H_3O^+ causes the shift of (00l) characteristic peak to a lower angle (6.87°), corresponding to the protonated product ($HNbWO_6$). After the self-assembly of MnTMPyP cations and the $[NbWO_6]^-$ nanosheets, the (00l) characteristic peak of the obtained MnTMPyP/$NbWO_6$ nanocomposites was shifted to 3.88°. According to the 2θ angle of the (00l) peaks, the basal spacing values of the three products can be calculated as 0.92 nm, 1.29 nm and 2.28 nm (Table 1), respectively. The interlayer spacing values (Δd) of the protonated product and the self-assembled product are calculated to be 0.53 nm and 1.52 nm by subtracting the thickness of $[NbWO_6]^-$ nanosheets (0.76 nm) [39]. Larger interlayer spacing indicates that the interlayer cations have been successfully inserted between the layers of the $[NbWO_6]^-$ nanosheets. In addition, the arrangement of MnTMPyP cations in the galley of the self-assembled product was further studied. Considering the size of the MnTMPyP cations (1.8 nm × 1.8 nm × 0.75 nm), one conclusion can be drawn that MnTMPyP cations are arranged at an angle of about 58° between the $[NbWO_6]^-$ nanosheets (Fig. S2).

Morphology analysis

The SEM images of $LiNbWO_6$, $HNbWO_6$ and MnTMPyP/$NbWO_6$ nanocomposites are shown in Fig. 2. As can be seen from Fig. 2a, the parent material $LiNbWO_6$ has a layered structure, and the layers are tightly arranged but irregular. Compared to the origin $LiNbWO_6$, the layered morphology of $HNbWO_6$ (Fig. 2b) was obtained by acid treatment with an obvious smooth surface. After the self-assembly of $[NbWO_6]^-$ nanosheets with manganese porphyrin cations, a two-dimensional layered structure was reconstructed. However, the surface of the resultant MnTMPyP/$NbWO_6$ nanocomposites (Fig. 2c) becomes rough and the edges of it are no longer neat and regular, which is due to a large number of TBA^+ cations and manganese porphyrin cations successively inserted between layers of $HNbWO_6$ through exfoliation/restacking process. The TEM image was performed in Fig. 2d to further certify the structure of the MnTMPyP/$NbWO_6$ nanocomposites, showing the clearly layered structure with many thin laminates. Furthermore, we also use AFM to study the morphology of the $[NbWO_6]^-$ nanosheets. As shown in Fig. S3, the nanosheets exhibit many irregular blocky, single-layer and flat morphology, and each of them has a lateral dimension of approximately hundreds of nanometers and a vertical dimension is less than 2 nm, which suggests the occurrence of exfoliation of acidification products.

Table 1 XRD data of the different samples

Compound	2θ (°)	d_{001} (nm)	Δd (nm)
$LiNbWO_6$	9.56	0.92	–
$HNbWO_6$	6.87	1.29	0.53
MnTMPyP/$NbWO_6$	3.88	2.28	1.52

Δd basal spacing-layer thickness (0.76 nm)

The element composition of the MnTMPyP/$NbWO_6$ nanocomposites was examined by high-angle annular dark-field scanning transmission electron microscopy (HAADF-STEM) and element mapping. In Fig. 3, there is a good spatial distribution corresponding to elements C, N, Mn which come from MnTMPyP cations and elements O, Nb, W which derived from the $[NbWO_6]^-$ nanosheets. It demonstrates that MnTMPyP cations and $[NbWO_6]^-$ nanosheets were recombined into a new MnTMPyP/$NbWO_6$ nanocomposites [40, 41]. Moreover, the elements analysis results of the MnTMPyP/$NbWO_6$ nanocomposites can be observed as follows: Mn (0.57 at.%), Nb (5.88 at.%) and W (7.55 at.%) (Table S1, Fig. S4). Therefore, we can infer that the chemical formula of MnTMPyP/$NbWO_6$ nanocomposites is $(MnTMPyP)_{0.08}H_{0.68}NbWO_6{\cdot}nH_2O$.

Zeta potential analysis

Zeta potential values of different volume ratios between MnTMPyP aqueous solution and $[NbWO_6]^-$ colloidal suspension were surveyed to further investigate the exfoliation/restacking process. As shown in Fig. S5, the Zeta potential value of $[NbWO_6]^-$ colloidal dispersion is − 45.7 mV, indicating the stable and well-dispersed niobium tungstate dispersion. As the volume ratio of MnTMPyP aqueous solution and $[NbWO_6]^-$ nanosheets is gradually increased (Fig. 4), the Zeta potential value of mixed solution increases and large amounts of dark brown flocculent precipitates can be seen. It illuminates that the assembly process of MnTMPyP/$NbWO_6$ nanocomposites is electrostatic force. When the volume ratio of MnTMPyP aqueous solution and

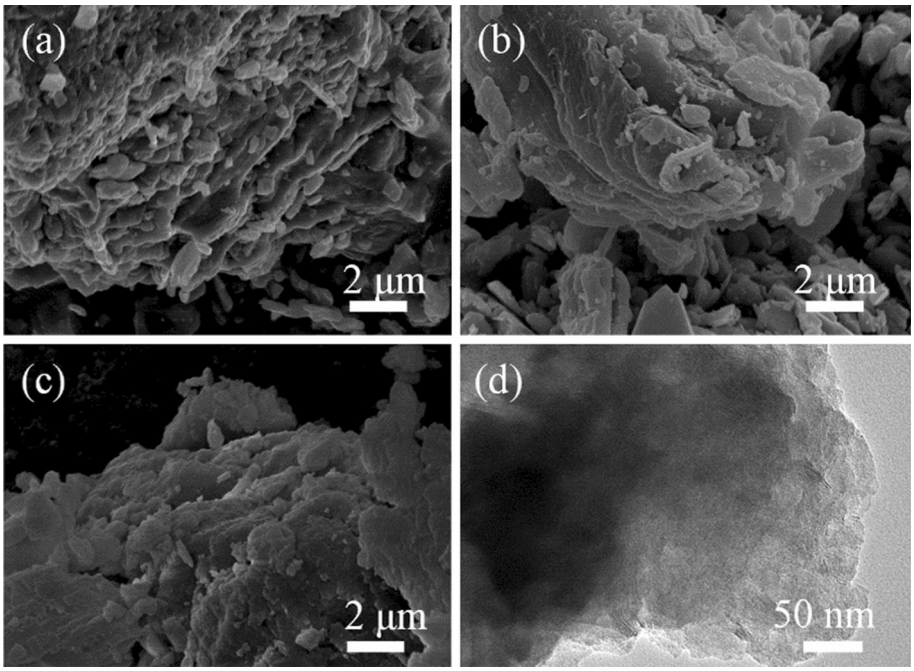

Figure 2 SEM images of **a** $LiNbWO_6$, **b** $HNbWO_6$ and **c** $MnTMPyP/NbWO_6$; TEM image of **d** $MnTMPyP/NbWO_6$.

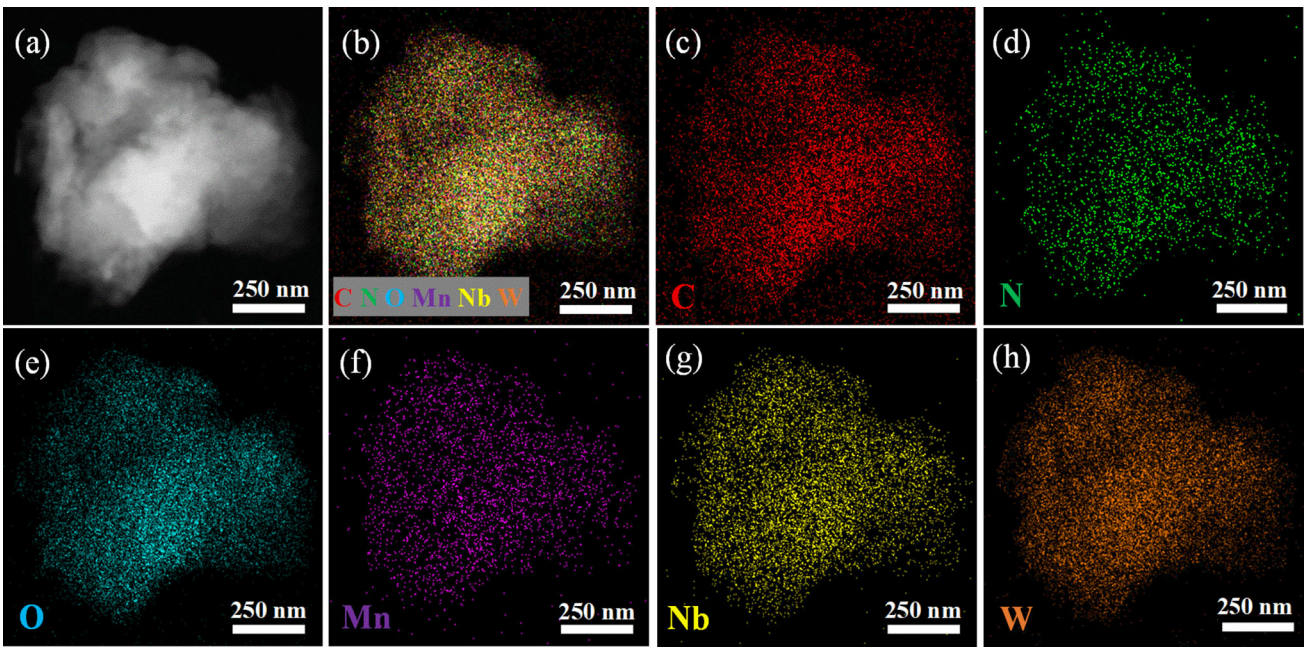

Figure 3 Element maps of the $MnTMPyP/NbWO_6$ nanocomposites by HAADF–STEM. **a** HAADF–STEM image of the $MnTMPyP/NbWO_6$ nanocomposites. **b** Combined C/N/O/Mn/Nb/W chemical maps of the $MnTMPyP/NbWO_6$ nanocomposites. The distribution of **c** C, **d** N, **e** O, **f** Mn, **g** Nb, and **h** W in the $MnTMPyP/NbWO_6$ nanocomposites.

$[NbWO_6]^-$ nanosheets is 1:2.7, the Zeta potential value reaches nearly zero (0.028 mV). Furthermore, the inset exhibits the Tyndall light scattering phenomenon of $[NbWO_6]^-$ nanosheets colloidal dispersion, suggesting the occurrence of exfoliation to a certain degree [42].

IR and UV–Vis spectra analysis

The FT-IR and UV–Vis tests were performed to further prove the preparation of $MnTMPyP/NbWO_6$ nanocomposites. The FT-IR spectra of $LiNbWO_6$, MnTMPyP and $MnTMPyP/NbWO_6$ can be observed

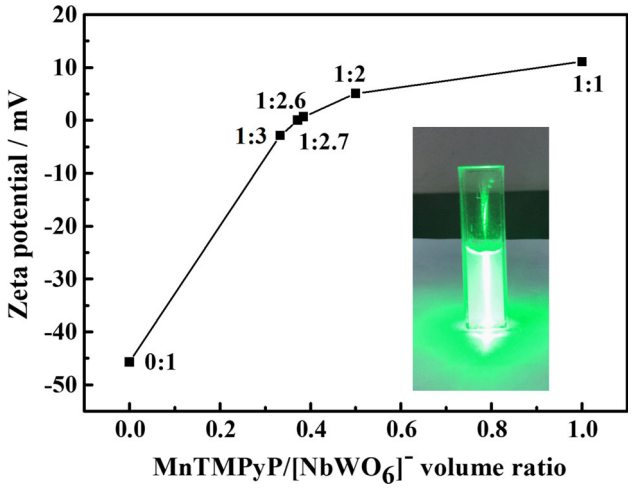

Figure 4 The relationship between Zeta potential and MnTMPyP/$[NbWO_6]^-$ volume ratio (the inset is Tyndall phenomenon of $[NbWO_6]^-$ nanosheets colloidal dispersion).

in Fig. 5a. The characteristic bands at 640 and 890 cm^{-1} in the $LiNbWO_6$ are attributed to Nb=O and O–W–O stretching vibration [43]. For MnTMPyP, the characteristic bands at 1641, 1465, 1385 and 1108 cm^{-1} are assigned to stretching vibration of C=N bonds in the pyridine substituent and stretching vibration of C=N, C=C and C–N bonds in the porphyrin rings, respectively [44]. Similarly, the absorption bands mentioned above can be observed in MnTMPyP/$NbWO_6$ nanocomposites, indicating that the hybrid contains both MnTMPyP cations and $[NbWO_6]^-$ nanosheets. However, compared with MnTMPyP and $[NbWO_6]^-$ nanosheets, these absorption bands are slightly offset because of the interaction between the two species.

As shown in Fig. 5b, UV–Vis absorption spectrum of MnTMPyP/$NbWO_6$ hybrid film shows a strong Soret band at 469 nm and a weak Q band at 570 nm. The Soret band and Q band of the hybrid film undergo redshift of 7 nm and 10 nm, respectively, owing to the strong interaction of MnTMPyP cations in the tight accumulation between the host material layers [37], comparing with the spectrum of MnTMPyP aqueous solution. Furthermore, the broadening phenomenon of the two absorption bands in the MnTMPyP/$NbWO_6$ nanocomposites may be due to the superposition and aggregation of metalloporphyrin cations between the $[NbWO_6]^-$ layers [35]. According to the above results, MnTMPyP cations were successfully inserted into the interlayer of $[NbWO_6]^-$ nanosheets.

Electrochemical characterization

The electrochemical behaviors of MnTMPyP/GCE and MnTMPyP/$NbWO_6$/GCE were performed in N_2-saturated 0.2 mol L^{-1} and pH 7.0 phosphate buffer solution (PBS) at a scan rate of 50 mV s^{-1} (Fig. 6a). For MnTMPyP/GCE, there is a couple of well-defined redox peaks at − 0.175 and − 0.259 V corresponding to a single electron reversible redox process of $Mn^{III}TMPyP^{5+}/Mn^{II}TMPyP^{4+}$ [26], and the potential difference between the two peaks (ΔE_p) is 84 mV. Similarity, a pair of redox peaks of MnTMPyP/$NbWO_6$/GCE appear at − 0.175 and − 0.238 V, respectively; the current of the redox peaks is larger than MnTMPyP and the ΔE_p reduces to 63 mV. This demonstrates that the semiconductor

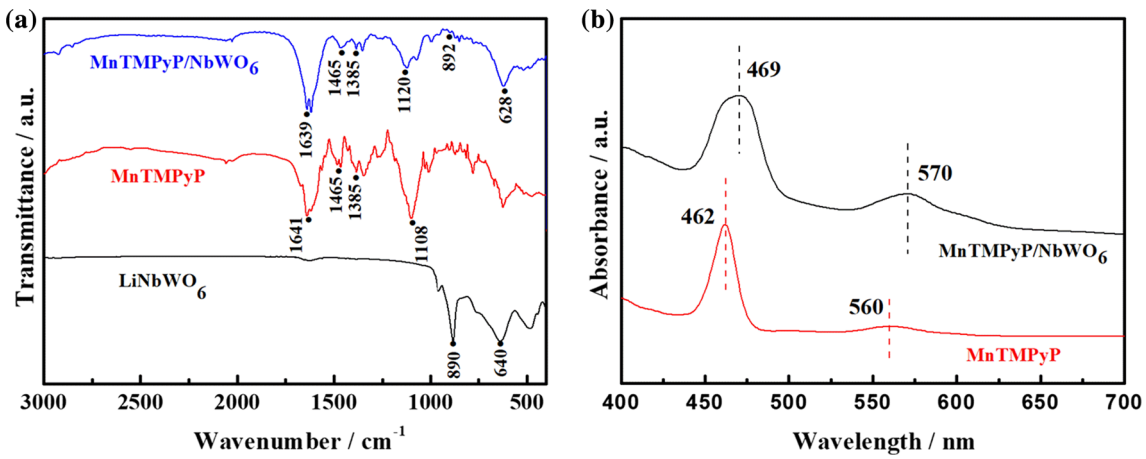

Figure 5 **a** FT-IR spectra of $LiNbWO_6$, MnTMPyP and MnTMPyP/$NbWO_6$; **b** UV–Vis absorption spectra of MnTMPyP aqueous solution and MnTMPyP/$NbWO_6$.

layers ($[NbWO_6]^-$ nanosheets) improve the electron transfer ability of MnTMPyP in the process of electrode testing [45].

The CV curves of MnTMPyP/$NbWO_6$/GCE measured at different scan rates in N_2-saturated pH 7.0 PBS are given in Fig. 6b. It can be clearly seen that the oxidation peaks and reduction peaks were moved toward the positive and negative directions, respectively, as the scan rate increasing. Meanwhile, the value of ΔE_p was increased from 63 to 112 mV as the scan rate increases from 50 to 250 mV s^{-1} due to the slow electron transfer process at high scan rates. Two linear relationships between anodic peak currents (I_{pa}), cathodic peak currents (I_{pc}) and the square root of the scan rate ($v^{1/2}$) are plotted in Fig. 6c. The liner equations are I_{pa} (μA) = − 14.97 + 2.92 $v^{1/2}$ ($v^{1/2}$ $s^{-1/2}$) (n = 7, $|R|$ = 0.9985) and I_{pc} (μA) = − 10.09 − 2.31 $v^{1/2}$ ($v^{1/2}$ $s^{-1/2}$) (n = 7, $|R|$ = 0.9986), indicating that the redox reaction of the hybrid undergoes a diffusion-controlled process. Here n and R represent the number of scans and linear correlation coefficients, respectively.

In order to investigate the electrochemical oxidation behavior of the modified electrode, a comprehensive comparison of the CV curves of bare electrode, $LiNbWO_6$/GCE, MnTMPyP/GCE and MnTMPyP/$NbWO_6$/GCE in N_2-saturated 0.2 mol L^{-1} and pH 7.0 PBS containing 6 mmol L^{-1} $NaNO_2$ at a scan rate of 100 mV s^{-1} is shown in Fig. 6d [46, 47]. There is a strong oxidation process on the surface of the four electrodes, which corresponds to a two-electron oxidation process from NO_2^- to NO_3^- [48]. However, the reduction process is absent in the reverse scan. This may be ascribed to the irreversibility of the electron transfer process and the coupling of fast irreversible post-electron-transfer chemical reactions [49]. Obviously, the oxidation

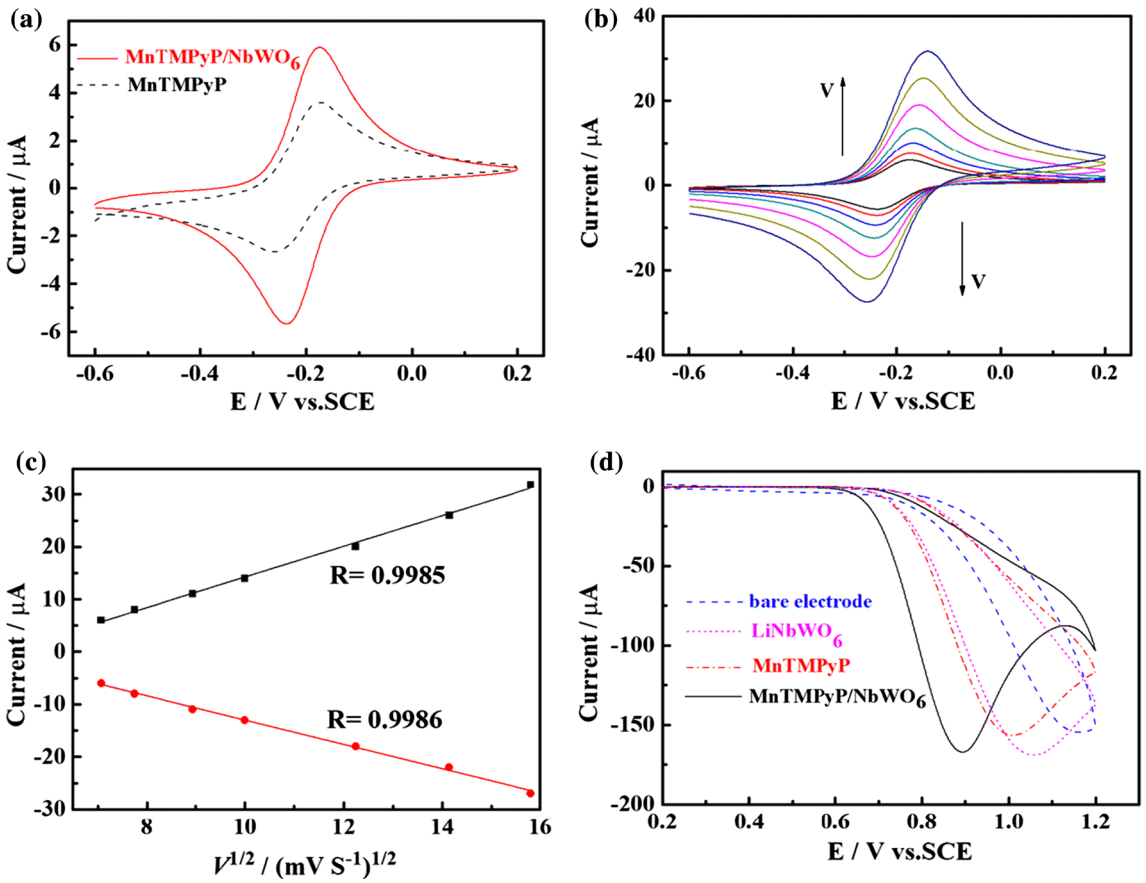

Figure 6 **a** CV curves of MnTMPyP/GCE (dash line) and CoTMPyP/$NbWO_6$/GCE (solid line) in N_2-saturated 0.2 mol L^{-1} and pH 7.0 PBS at a scan rate of 50 mV s^{-1}; **b** CV curves of CoTMPyP/$NbWO_6$/GCE in N_2-saturated pH 7.0 PBS at 50, 60, 80, 100, 150, 200, 250 mV s^{-1} from inner to outer; **c** the linear relationship between I and $v^{1/2}$; **d** CV curves of bare electrode (dash line), $LiNbWO_6$/GCE (short dash line), MnTMPyP/GCE (dash dot line) and MnTMPyP/$NbWO_6$/GCE (solid line) in N_2-saturated 0.2 mol L^{-1} and pH 7.0 PBS containing 6 mmol L^{-1} $NaNO_2$ at a scan rate of 100 mV s^{-1}.

peak potential (E_{pa}) of the MnTMPyP/$NbWO_6$/GCE moves toward negative than bare electrode, indicating the electro-catalytic oxidation of nitrite. On the one hand, the E_{pa} values of the MnTMPyP/$NbWO_6$/GCE (0.89 V) were negatively shifted to 270, 170 and 120 mV, respectively, compared with that of the bare electrode (1.16 V), $LiNbWO_6$/GCE (1.06 V) and MnTMPyP/GCE (1.01 V). On the other hand, the oxidation peak current of the MnTMPyP/$NbWO_6$/GCE is relatively high. All the characteristics mentioned above are electrochemical catalytic oxidation process, suggesting that the MnTMPyP/$NbWO_6$ nanocomposites can enhance electro-catalytic oxidation of nitrite efficiently.

As illustrated in Fig. 7a, the influence of the scan rate on MnTMPyP/$NbWO_6$/GCE oxidation peak current was studied by CV curves in PBS containing 6 mmol L^{-1} $NaNO_2$ at the scan rate range of 10–150 mV s^{-1}. With the increase in the scan rate, the value of E_{pa} was positively moved and the I_{pa} was gradually increased. Additionally, the I_{pa} is proportional to the $v^{1/2}$, indicating that the electro-catalytic oxidation of nitrite on the surface of MnTMPyP/$NbWO_6$/GCE is a typical diffusion-controlled process. The linear relationship between I_{pa} and E_{pa} is displayed in Fig. 7b, and the liner equations can be expressed as I_{pa} (μA) = 21.2 − 18.9 $v^{1/2}$ ($v^{1/2}$ $s^{-1/2}$) (n = 10, $|R|$ = 0.9993). According to previous studies [50], the electro-catalytic mechanism of nitrite oxidation on MnTMPyP/$NbWO_6$/GCE is proposed as follows:

$$Mn^{III}TMPyP^{5+} + NO_2^- \rightleftarrows \left[Mn^{II}TMPyP\ (NO_2)\right]^{4+} \quad (1)$$

$$\left[Mn^{II}TMPyP\ (NO_2)\right]^{4+} \rightleftarrows Mn^{III}TMPyP^{5+} + NO_2 + e^- \quad (2)$$

$$2\ NO_2 + H_2O \rightleftarrows 2\ H^+ + NO_3^- + NO_2^- \quad (3)$$

$$NO_2^- + H_2O \rightarrow 2\ H^+ + NO_3^- + 2\ e^- \quad (4)$$

According to the characteristic that DPV technology is sensitive to nitrite detection. Hence, this technology was conducted for the quantitative determination of nitrite on the MnTMPyP/$NbWO_6$/GCE. In N_2-saturated 0.2 mol L^{-1} and pH 7.0 PBS with different concentrations of $NaNO_2$, DPVs of $NaNO_2$ at MnTMPyP/$NbWO_6$/GCE are presented in Fig. 7c. With gradient concentrations of $NaNO_2$ from 1.20×10^{-4} to 3.57×10^{-3} mol L^{-1}, the oxidation peak current increases gradually and the oxidation peak potential moves toward high potential. In Fig. 7d, a linear regression equation between the peak current (I_{pa}) and the concentration (C) can be obtained as I_{pa} (μA) = 2.94 C + 0.40 (C) (mmol L^{-1}) (n = 12, $|R|$ = 0.9998), with a detection limit of 3.80×10^{-5} mol L^{-1} at a signal-to-noise ratio of 3.0 [34]. Moreover, the comparison with some previously reported tests for nitrite is listed in Table 2. It can be observed that the MnTMPyP/$NbWO_6$/GCE has a great detection performance for the electro-catalytic oxidation of nitrite.

Stability and reproducibility of the MnTMPyP/$NbWO_6$/GCE

For evaluating the stability and reproducibility of the MnTMPyP/$NbWO_6$/GCE, a string of DPV measurements were taken in N_2-saturated 0.2 mol L^{-1} and pH 7.0 PBS containing 2.47 mmol L^{-1} $NaNO_2$. In Fig. 8a, this bar chart reflects the results of ten consecutive measurements with little change in current, and the relative standard deviation (RSD) is calculated to be 0.74%. Moreover, the stability test of $NaNO_2$ at the MnTMPyP/$NbWO_6$/GCE within 1 month is displayed in Fig. 8b. After 9 days of storage, the peak current was decreased by only 1.53%. And the current value was still retained 88.18% for a month later. Meanwhile, the hybrid thin film on the modified electrode can be continuously tested for several hours without shedding in the process of electrochemical measurement. These research results suggest that the excellent stability of the MnTMPyP/$NbWO_6$/GCE enables it to be subjected to extensive testing. In addition, from Fig. 8c, the reproducibility of the MnTMPyP/$NbWO_6$/GCE was also investigated at five different electrodes with the RSD of 0.3%. The great reproducibility indicates that the fabrication of the MnTMPyP/$NbWO_6$ nanocomposites is credible.

Interference

The selectivity and suitability of the senor built on MnTMPyP/$NbWO_6$ nanocomposites were assessed by comparing it with some common substances related to food and environment, including AA, Glucose, KCl, $NaNO_3$, and NaCl. As shown in

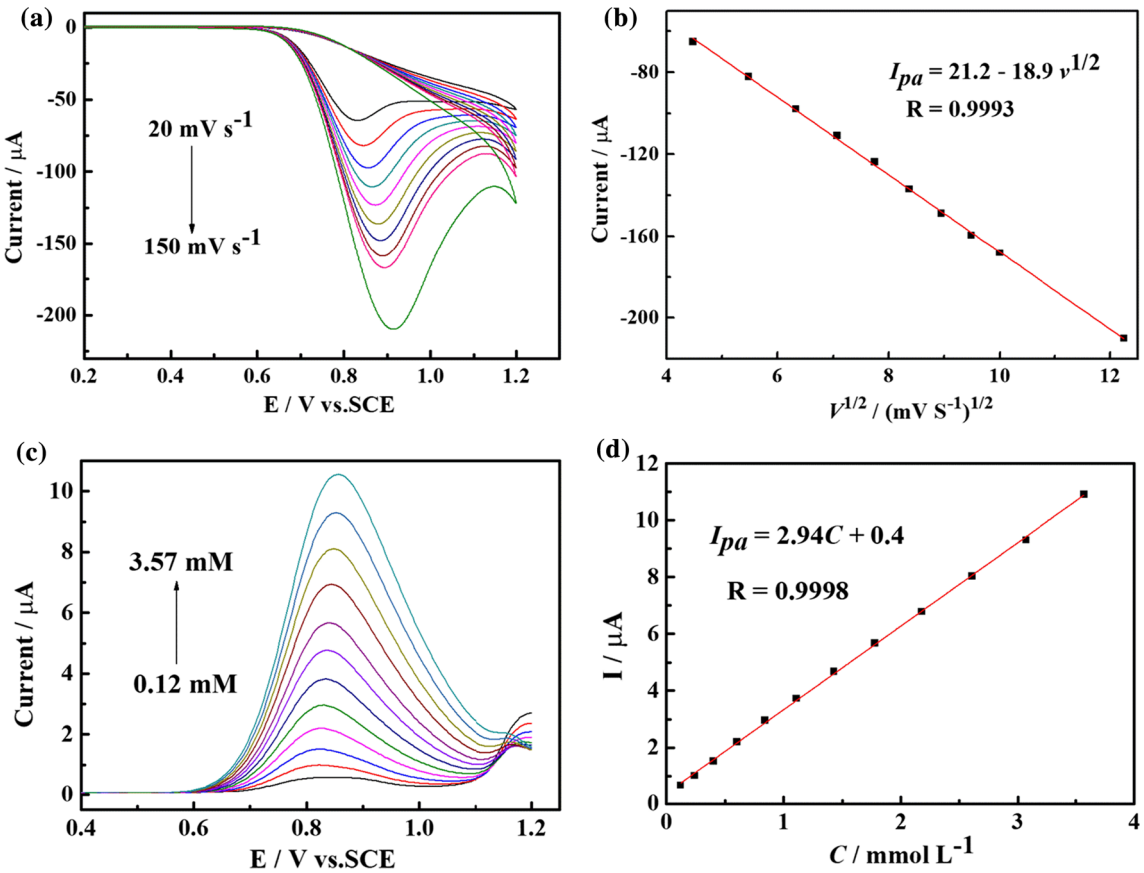

Figure 7 **a** CV curves of MnTMPyP/$NbWO_6$/GCE in N_2-saturated 0.2 mol L^{-1} and pH 7.0 PBS containing 6 mmol L^{-1} $NaNO_2$ at scan rates of 20,30,40, 50, 60, 70, 80, 90, 100 and 150 mV s^{-1}; **b** the relationship curve between the oxidation peak current (I_{pa}) and the square root of scan rate ($v^{1/2}$); **c** DPV curves of MnTMPyP/$NbWO_6$/GCE in N_2-saturated 0.2 mol L^{-1} and pH 7.0 PBS with different concentrations of $NaNO_2$; **d** the relationship between $NaNO_2$ concentration (C) and oxidation peak current (I_{pa}).

Table 2 Comparison for determination of $NaNO_2$ at different modified electrodes

Electrode material	Limit (mol L^{-1})	Linger range (mmol L^{-1})	References
ASCA	2.1×10^{-4}	0.1–4.0	[51]
Poly (ortho-toluidine)	3.4×10^{-4}	0.5–19	[52]
MnTMPyP/ZrP	5.3×10^{-5}	0.15–4.76	[53]
RGO/MWNTs	2.5×10^{-5}	0.075–6.06	[54]
Pt–Fe	3.0×10^{-5}	1.0–50	[55]
MnTMPyP/$LiNbWO_6$	3.8×10^{-5}	0.12–3.57	This work

Fig. 8d, the concentrations of these possible interferents are 100-fold than $NaNO_2$, and the current response changes are calculated to be 4.6, 4.2, 3.0, 5.1 and 3.1%, respectively. These interferents show the little effect on the determination of nitrite, demonstrating that the sensor has a strong anti-interference ability.

Conclusions

In this work, the MnTMPyP/$NbWO_6$ nanocomposites were fabricated through a rapid and convenient self-assembly method. The element composition and structure of the nanocomposites were confirmed by XRD, SEM, HAADF-STEM, EDS, UV–Vis and IR. Herein, a novel electrochemical sensor based on MnTMPyP/$NbWO_6$ nanocomposites held the

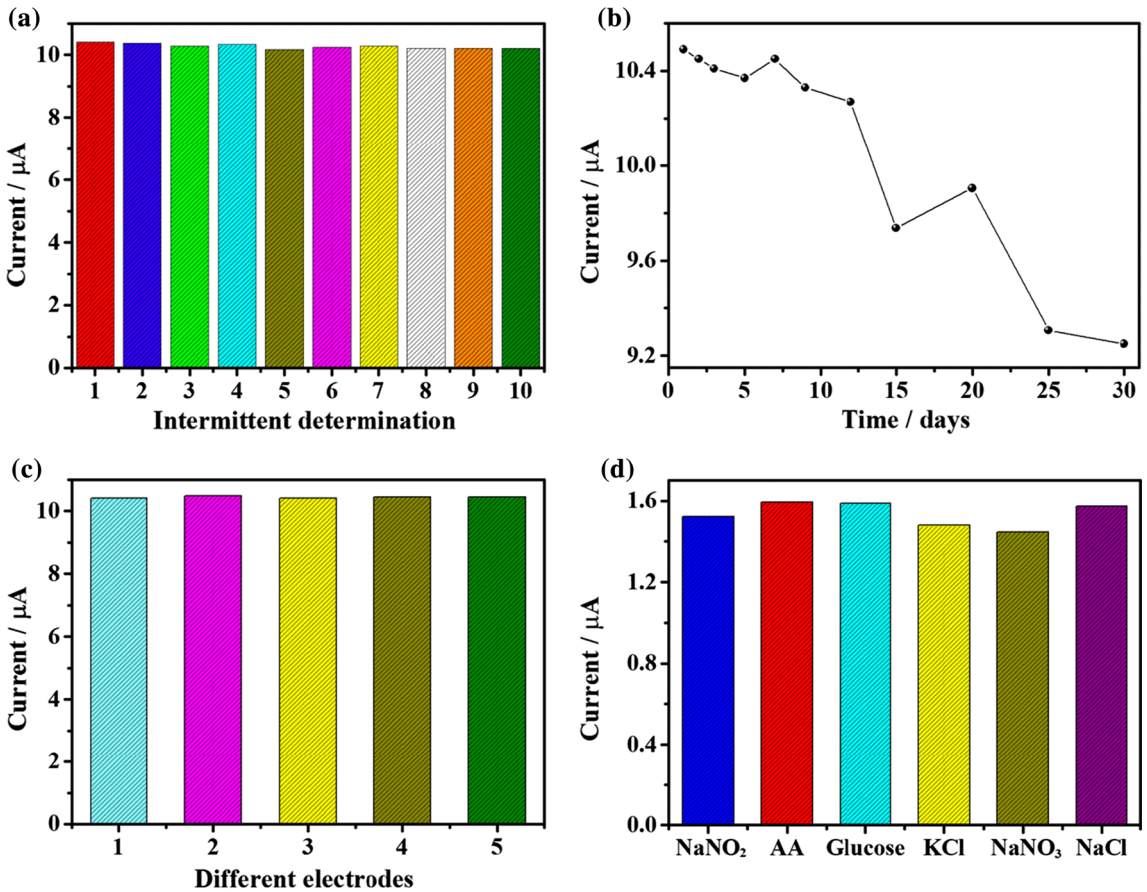

Figure 8 **a** The oxidation currents of repetitive determinations on $MnTMPyP/NbWO_6$/GCE in N_2-saturated 0.2 mol L^{-1} and pH 7.0 PBS containing 2.47 mmol L^{-1} $NaNO_2$; **b** the oxidation peak currents of 2.47 mmol L^{-1} $NaNO_2$ detected at different storage times; **c** the oxidation currents of 2.47 mmol L^{-1} $NaNO_2$ at different electrodes; **d** the oxidation peak currents of 0.22 mmol L^{-1} $NaNO_2$ detected with 100-fold interference species of AA, Glucose, KCl, $NaNO_3$, and NaCl.

capacity for the detection of nitrite. From the results of CVs and DPVs of the proposed modified GCE, the sensor exhibited excellent electro-catalytic oxidation activity toward nitrite and a great detection limit of 3.80×10^{-5} mol L^{-1} in neutral solution. Furthermore, the sensitivity, stability, reproducibility and anti-interference of the prepared sensor were also displayed remarkable. Therefore, the electrochemical detection method could serve as a simple, sensitive, stable and repeatable assay to determine nitrite. It is significant for the sensor to be applied to the environmental sample analysis.

Acknowledgements

This work was supported by Natural Science Foundation of Jiangsu Province (BK20161294, BK20160434), Lianyungang Science Project (CG1602), the University Science Research Project of Jiangsu Province (15KJB430004), Postgraduate Research and Practice Innovation Program of Jiangsu Province (KYCX18_2607), the Jiangsu Marine Resources Development and Research Institute (LYG52105-2018045), China Postdoctoral Science Foundation (2018M632283), Industry-University-Research Collaboration Project of Jiangsu Province (BY2018281), and Huaihai Institute of Technology Graduate Practice Innovation Project (XKYCXX2017-5).

Compliance with ethical standards

Conflict of interest All authors declare that they have no conflict of interest.

Electronic supplementary material: The online version of this article (https://doi.org/10.1007/s108

53-019-03526-4) contains supplementary material, which is available to authorized users.

References

[1] Rosca V, Duca M, de Groot MT, Koper MT (2009) Nitrogen cycle electrocatalysis. Chem Rev 109:2209–2244

[2] Zhang ML, Huang DK, Cao Z, Liu YQ, He JL, Xiong JF, Yin YL (2015) Determination of trace nitrite in pickled food with a nano-composite electrode by electrodepositing ZnO and Pt nanoparticles on MWCNTs substrate. LWT Food Sci Technol 64:663–670

[3] Daniel WL, Han MS, Lee JS, Mirkin CA (2009) Colorimetric nitrite and nitrate detection with gold nanoparticle probes and kinetic end points. J Am Chem Soc 131:6362–6363

[4] Wu L, Zhang X, Wang M, He L, Zhang Z (2018) Preparation of Cu_2O/CNTs composite and its application as sensing platform for detecting nitrite in water environment. Measurement 128:189–196

[5] Wang H, Wan N, Ma L, Wang Z, Cui B, Han W, Chen Y (2018) A novel and simple spectrophotometric method for detection of nitrite in water. Analyst 143:4555–4558

[6] Hussain I, Ahamad KU, Nath P (2016) Low-cost, robust, and field portable smartphone platform photometric sensor for fluoride level detection in drinking water. Anal Chem 89:767–775

[7] Zhu N, Xu Q, Li S, Gao H (2009) Electrochemical determination of nitrite based on poly (amidoamine) dendrimer-modified carbon nanotubes for nitrite oxidation. Electrochem Commun 11:2308–2311

[8] Liu QH, Yan XL, Guo JC, Wang DH, Lei L, Yan FY, Chen LG (2009) Spectrofluorimetric determination of trace nitrite with a novel fluorescent probe. Spectrochim Acta 73:789–793

[9] Zhang Y, Su Z, Li B, Zhang L, Fan D, Ma H (2016) Recyclable magnetic mesoporous nanocomposite with improved sensing performance toward nitrite. ACS Appl Mater Int 8:12344–12351

[10] Yue XF, Zhang ZQ, Yan HT (2004) Flow injection catalytic spectrophotometric simultaneous determination of nitrite and nitrate. Talanta 62:97–101

[11] Kikura-Hanajiri R, Martin RS, Lunte SM (2002) Indirect measurement of nitric oxide production by monitoring nitrate and nitrite using microchip electrophoresis with electrochemical detection. Anal Chem 74:6370–6377

[12] Tsikas D (2000) Simultaneous derivatization and quantification of the nitric oxide metabolites nitrite and nitrate in biological fluids by gas chromatography/mass spectrometry. Anal Chem 72:4064–4072

[13] Rajalakshmi K, John SA (2015) Highly sensitive determination of nitrite using FMWCNTs-conducting polymer composite modified electrode. Sens Actuators B Chem 215:119–124

[14] Zhang S, Li B, Sheng Q, Zheng J (2016) Electrochemical sensor for sensitive determination of nitrite based on the CuS–MWCNT nanocomposites. J Electroanal Chem 769:118–123

[15] Mani V, Periasamy AP, Chen SM (2012) Highly selective amperometric nitrite sensor based on chemically reduced graphene oxide modified electrode. Electrochem Commun 17:75–78

[16] Liu C, Zhu H, Zhu Y, Dong P, Hou H, Xu Q, Hou W (2018) Ordered layered N-doped $KTiNbO_5/gC_3N_4$ heterojunction with enhanced visible light photocatalytic activity. Appl Catal B Environ 228:54–63

[17] Li J, Zhang X, Pan B, Xu J, Liu L, Ma J, Tong Z (2016) Application of a nanostructured composite material constructed by self-assembly of titanoniobate nanosheets and cobalt porphyrin to electrocatalytic reduction of oxygen. Chin J Chem 34:1021–1026

[18] Liu C, Zhang C, Wang J, Xu Q, Chen X, Wang C, Hou W (2018) N-doped $CsTi_2NbO_7@gC_3N_4$ core–shell nanobelts with enhanced visible light photocatalytic activity. Mater Lett 217:235–238

[19] Li J, Pan B, Xu J, Wang M, Zhang X, Liu L, Tong Z (2017) Nanotubes formed by exfoliation of $HTaWO_6$. Chem Lett 46:597–598

[20] Ali Z, Khan I, Rahman M, Ahmad R, Ahmad I (2016) Electronic structure of the $LiAA'O_6$ (A = Nb, Ta, and A' = W, Mo) ceramics by modified Becke–Johnson potential. Opt Mater 58:466–475

[21] Pan B, Xu J, Zhang X, Li J, Wang M, Ma J, Tong Z (2018) Electrostatic self-assembly behaviour of exfoliated $Sr_2Nb_3O_{10}^-$ nanosheets and cobalt porphyrins: exploration of non-noble electro-catalysts towards hydrazine hydrate oxidation. J Mater Sci 53:6494–6504. https://doi.org/10.1007/s10853-018-2033-x

[22] Sun Y, Deng JP, Tu ZY, Ma JJ (2016) Preparation and electrochemical performance of manganese porphyrin/titanate intercalated nanocomposite. Mater Sci Eng 137:012031

[23] Xu J, Pan B, Li J, Zhang X, Wang M, Tong Z (2017) Electrocatalytic activity towards oxygen reduction reaction of laminar nanocomposite $LaNb_2O_7/Co^{III}$TMPyP prepared via the exfoliation/restacking method. Micro Nano Lett 12:731–734

[24] Miyamoto N, Yamamoto H, Kaito R, Kuroda K (2002) Formation of extraordinarily large nanosheets from $K_4Nb_6O_{17}$ crystals. Chem Commun 0:2378–2379

[25] Bizeto MA, Shiguihara AL, Constantino VR (2009) Layered niobate nanosheets: building blocks for advanced materials assembly. J Mater Chem 19:2512–2525

[26] Ma J, Yang M, Chen Y, Liu L, Zhang X, Wang M, Tong Z (2015) Sandwich-structured composite from the direct coassembly of layered titanate nanosheets and Mn porphyrin and its electrocatalytic performance for nitrite oxidation. Mater Lett 150:122–125

[27] Ma J, Zhang Z, Yang M, Wu Y, Feng X, Liu L, Tong Z (2016) Intercalated methylene blue between calcium niobate nanosheets by ESD technique for electrocatalytic oxidation of ascorbic acid. Microporous Mesoporous Mater 221:123–127

[28] Xu J, Wang M, Pan B, Li J, Xia B, Zhang X, Tong Z (2017) Electrostatic self-assembly of exfoliated niobate nanosheets ($Nb_3O_8^-$) and cobalt porphyrins ($Co^{III}TMPyP$) utilized for rapid construction of intercalated nanocomposite and exploration of electrocatalysis towards oxygen reduction. Funct Mater Lett 10:1750070

[29] Kung CW, Chang TH, Chou LY, Hupp JT, Farha OK, Ho KC (2015) Porphyrin-based metal–organic framework thin films for electrochemical nitrite detection. Electrochem Commun 58:51–56

[30] Wu H, Fan S, Jin X, Zhang H, Chen H, Dai Z, Zou X (2014) Construction of a zinc porphyrin-fullerene-derivative based nonenzymatic electrochemical sensor for sensitive sensing of hydrogen peroxide and nitrite. Anal Chem 86:6285–6290

[31] Kemmegne-Mbouguen JC, Angnes L (2015) Simultaneous quantification of ascorbic acid, uric acid and nitrite using a clay/porphyrin modified electrode. Sens Actuators B Chem 212:464–471

[32] Winnischofer H, de Souza Lima S, Araki K, Toma HE (2003) Electrocatalytic activity of a new nanostructured polymeric tetraruthenated porphyrin film for nitrite detection. Anal Chim Acta 480:97–107

[33] Xu J, Xia B, Wang M, Fan Z, Zhang X, Ma J, Tong Z (2018) A biosensor consisting of $Ca_2Nb_3O_{10}^-$ substrates and functional molecule manganese porphyrins (MnTMPyP) utilized for the determinations of nitrite. Funct Mater Lett 11:1850053

[34] Wang M, Liu Y, Zhang X, Fan Z, Tong Z (2018) Development of sandwich-structured cobalt porphyrin/niobium molybdate nanosheets catalyst for oxygen reduction. J Mater Res 33:4199–4206

[35] Wang M, Xu J, Zhang X, Fan Z, Tong Z (2018) Fabrication of a new self-assembly compound of $CsTi_2NbO_7$ with cationic cobalt porphyrin utilized as an ascorbic acid sensor. Appl Biochem Biotechnol 185:834–846

[36] Hu LF, Li R, He J, Da LG, Lv W, Hu JS (2015) Structure and photocatalytic performance of layered $HNbWO_6$ nanosheet aggregation. J Nanophotonics 9:093041

[37] Pan B, Zhao W, Zhang X, Li J, Xu J, Ma J, Tong Z (2016) Research on the self-assembly of exfoliated perovskite nanosheets ($LaNb_2O_7^-$) and cobalt porphyrin utilized for the electrocatalytic oxidation of ascorbic acid. RSC Adv 6:46388–46393

[38] He J, Li QJ, Tang Y, Yang P, Li A, Li R, Li HZ (2012) Characterization of $HNbMoO_6$, $HNbWO_6$ and $HTiNbO_5$ as solid acids and their catalytic properties for esterification reaction. Appl Catal A Gen 443:145–152

[39] Prasad GK, Takei T, Arimoto K, Yonesaki Y, Kumada N, Kinomura N (2006) Nanocomposites based on exfoliated $NbWO_6$ nanosheets and ionic polyacetylenes. Solid State Ionics 177:197–201

[40] Luo B, Chen M, Zhang Z, Xu J, Li D, Xu D, Shi W (2017) Highly efficient visible-light-driven photocatalytic degradation of tetracycline by a Z-scheme gC_3N_4/Bi_3TaO_7 nanocomposite photocatalyst. Dalton Trans 46:8431–8438

[41] Liu C, Wu Q, Ji M, Zhu H, Hou H, Yang Q, Hou W (2017) Constructing Z-scheme charge separation in 2D layered porous BiOBr/graphitic C_3N_4 nanosheets nanojunction with enhanced photocatalytic activity. J Alloy Compd 723:1121–1131

[42] Liu Z, Ma R, Osada M, Iyi N, Ebina Y, Takada K, Sasaki T (2006) Synthesis, anion exchange, and delamination of Co–Al layered double hydroxide: assembly of the exfoliated nanosheet/polyanion composite films and magneto-optical studies. J Am Chem Soc 128:4872–4880

[43] Wang Y, Dong R, Li A, Hu LF, He J (2016) Characterization of modified α-$LiNbWO_6$ layered materials and their catalytic performance for toluene nitration. Optoelectron Adv Mater 10:102–107

[44] Tao T, Zhang X, Liu L, Ma J, Zhang D, Pan B, Tong Z (2014) Preparation and electrochemical behaviour study of layered $Bi_2SrTa_2O_9$ with a cationic manganese porphyrin. Micro Nano Lett 9:909–912

[45] Ma J, Wu J, Zheng J, Liu L, Zhang D, Xu X, Tong Z (2012) Synthesis, characterization and electrochemical behavior of cationic iron porphyrin intercalated into layered niobite. Microporous Mesoporous Mater 151:325–329

[46] Wu M, Wang Y, Wei Z, Wang L, Zhuo M, Zhang J, Ma J (2018) Ternary doped porous carbon nanofibers with excellent ORR and OER performance for zinc–air batteries. J Mater Chem A 6:10918–10925

[47] Wang L, Wang Y, Wu M, Wei Z, Cui C, Mao M, Ma J (2018) Nitrogen, fluorine, and boron ternary doped carbon

fibers as cathode electrocatalysts for zinc–air batteries. Small 14:1800737

[48] Sousa AL, Santos WJ, Luz RC, Damos FS, Kubota LT, Tanaka AA, Tanaka SM (2008) Amperometric sensor for nitrite based on copper tetrasulphonated phthalocyanine immobilized with poly-L-lysine film. Talanta 75:333–338

[49] Zhang X, Wang M, Li D, Liu L, Ma J, Gong J, Tong Z (2013) Electrochemical investigation of a novel metalloporphyrin intercalated layered niobate modified electrode and its electrocatalysis on ascorbic acid. J Solid State Electron 17:3177–3184

[50] Armijo F, Goya MC, Reina M, Canales MJ, Arévalo MC, Aguirre MJ (2007) Electrocatalytic oxidation of nitrite to nitrate mediated by Fe(III) poly-3-aminophenyl porphyrin grown on five different electrode surfaces. J Mol Catal A Chem 268:148–154

[51] do Carmo DR, Paim LL, Metzker G, Dias Filho NL, Stradiotto NR (2010) A novel nanostructured composite formed by interaction of copper octa (3-aminopropyl) octasilsesquioxane with azide ligands: preparation, characterization and a voltammetric application. Mater Res Bull 45:1263–1270

[52] Ojani R, Raoof JB, Zarei E (2008) Poly (ortho-toluidine) modified carbon paste electrode: a sensor for electrocatalytic reduction of nitrite. Electroanalysis 20:379–385

[53] Pan B, Ma J, Zhang X, Li J, Liu L, Zhang D, Tong Z (2015) A laminar nanocomposite constructed by self-assembly of exfoliated α-ZrP nanosheets and manganese porphyrin for use in the electrocatalytic oxidation of nitrite. J Mater Sci 50:6469–6476. https://doi.org/10.1007/s10853-015-9205-8

[54] Hu F, Chen S, Wang C, Yuan R, Yuan D, Wang C (2012) Study on the application of reduced graphene oxide and multiwall carbon nanotubes hybrid materials for simultaneous determination of catechol, hydroquinone, p-cresol and nitrite. Anal Chim Acta 724:40–46

[55] Liu SY, Chen YP, Fang F et al (2008) Innovative solid-state microelectrode for nitrite determination in a nitrifying granule. Environ Sci Technol 42:4467–4471